ARTICLE IN PRESS

Energy Storage Materials xxx (xxxx) xxx

Contents lists available at ScienceDirect

Energy Storage Materials

journal homepage: www.elsevier.com/locate/ensm

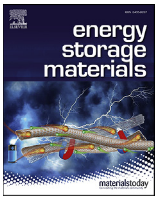

A Novel Ni-rich O3-Na[$Ni_{0.60}Fe_{0.25}Mn_{0.15}$]$O_2$ Cathode for Na-ion Batteries

Feixiang Ding [a,b,#], Chenglong Zhao [a,b,#], Dong Zhou [c], Qingshi Meng [a,b], Dongdong Xiao [d], Qiangqiang Zhang [a,b], Yaoshen Niu [a,b], Yuqi Li [a,b], Xiaohui Rong [a,b,**], Yaxiang Lu [a,e,***], Liquan Chen [a,e], Yong-Sheng Hu [a,b,e,*]

[a] *Key Laboratory for Renewable Energy, Beijing Key Laboratory for New Energy Materials and Devices, Beijing National Laboratory for Condensed Matter, Physics Institute of Physics, Chinese Academy of Sciences, Beijing, 100190, China*
[b] *Center of Materials Science and Optoelectronics Engineering, University of Chinese Academy of Sciences, China*
[c] *Helmholtz Zentrum Berlin für Materialien und Energie, Hahn-Meitner-Platz 1, Berlin, 14109, Germany*
[d] *Beijing National Laboratory for Condensed Matter Physics, Institute of Physics Chinese Academy of Sciences, Beijing, 100049, China*
[e] *Yangtze River Delta Physics Research Center Co. Ltd, Liyang, 213300, China*

ARTICLE INFO

Keywords:
Ni-rich O3 cathode
High-voltage phase
Phase evolution
Na[$Ni_{0.60}Fe_{0.25}Mn_{0.15}$]$O_2$
Na-ion battery

ABSTRACT

O3-type layered oxide materials are being considered as one of the most promising cathodes for Na-ion batteries owing to their higher capacity, however, they usually suffer from structural damage at the highly desodiated state. To achieve the stable/high-capacity O3-type Na-ion cathodes, a series of Ni-rich O3–Na[$Ni_xFe_yMn_{1-x-y}$]O_2 (x = 0.6, 0.7 and 0.8) oxide cathodes were successfully prepared and the phase transitions at high voltage were systematically investigated. Combined with the electrochemical measurements and structural characterizations, the structural transitions from O3 to O′3, P3, O3″ phases during the Na^+ (de)intercalation process were demonstrated in the voltage range of 2.0–4.2 V. Moreover, several reasons for the high-voltage capacity decay are revealed: 1) the thermodynamic instability of high-voltage phase due to less Na^+ in the crystal structure; 2) large volume change during the high-voltage phase evolution with inferior Na^+ diffusion kinetics; 3) formation of microcracks and cathode-electrolyte interphase on the surface of cathode particles. To address the above issues, a reasonable upper cut-off voltage of 4.0 V was set to prevent the formation of O3″ phase and reduce electrolyte decomposition, which leads to a high reversible capacity of ~152 mAh g^{-1} (~467 Wh kg^{-1}) with a superior capacity retention of ~84% after 200 cycles at 0.5C, showing great Na storage performance. This work provides insights on the relationship of the structure-property for the further development of high-performance Ni-rich O3-type Na-ion cathodes.

1. Introduction

Na-ion batteries (NIBs) have experienced a considerable development during the past decade, for which NIBs are believed to be the promising supplement to Li-ion batteries (LIBs) for the abundant sodium resources in large-scale energy storage applications [1–3]. Until now, great efforts have been devoted to developing high-performance cathode materials, including layered oxides [4–8], polyanionic compounds [9–11], and Prussian blue analogues [12–14]. Among the Na-intercalation cathode materials, O3-type layered transition metal (TM) oxides of Na_xTMO_2 (x~1.0) are considered as one of most promising type, owing to their high specific capacity and flexible synthesis process [3,15].

Ni-rich O3-type Na_xTMO_2 materials with high capacity have been widely studied. As a starting material, monoclinic $NaNiO_2$ (O′3 phase) shows the charged capacity of ~190 mAh g^{-1} but with reversible discharged capacity of 147 mAh g^{-1} when cycling in 2.0–4.5 V [16] as

---

[*] Corresponding author. Key Laboratory for Renewable Energy, Beijing Key Laboratory for New Energy Materials and Devices, Beijing National Laboratory for Condensed Matter, Physics Institute of Physics, Chinese Academy of Sciences, Beijing, 100190, China.
[**] Corresponding author. Key Laboratory for Renewable Energy, Beijing Key Laboratory for New Energy Materials and Devices, Beijing National Laboratory for Condensed Matter, Physics Institute of Physics, Chinese Academy of Sciences, Beijing, 100190, China.
[***] Corresponding author. Key Laboratory for Renewable Energy, Beijing Key Laboratory for New Energy Materials and Devices, Beijing National Laboratory for Condensed Matter, Physics Institute of Physics, Chinese Academy of Sciences, Beijing, 100190, China.
E-mail addresses: rongxiaohui123@126.com (X. Rong), yxlu@iphy.ac.cn (Y. Lu), yshu@iphy.ac.cn (Y.-S. Hu).
[#] These authors contributed equally to this work.

https://doi.org/10.1016/j.ensm.2020.05.013
Received 29 April 2020; Accepted 14 May 2020
Available online xxxx
2405-8297/© 2020 Elsevier B.V. All rights reserved.

Please cite this article as: F. Ding et al., A Novel Ni-rich O3-Na[$Ni_{0.60}Fe_{0.25}Mn_{0.15}$]$O_2$ Cathode for Na-ion Batteries, Energy Storage Materials, https://doi.org/10.1016/j.ensm.2020.05.013

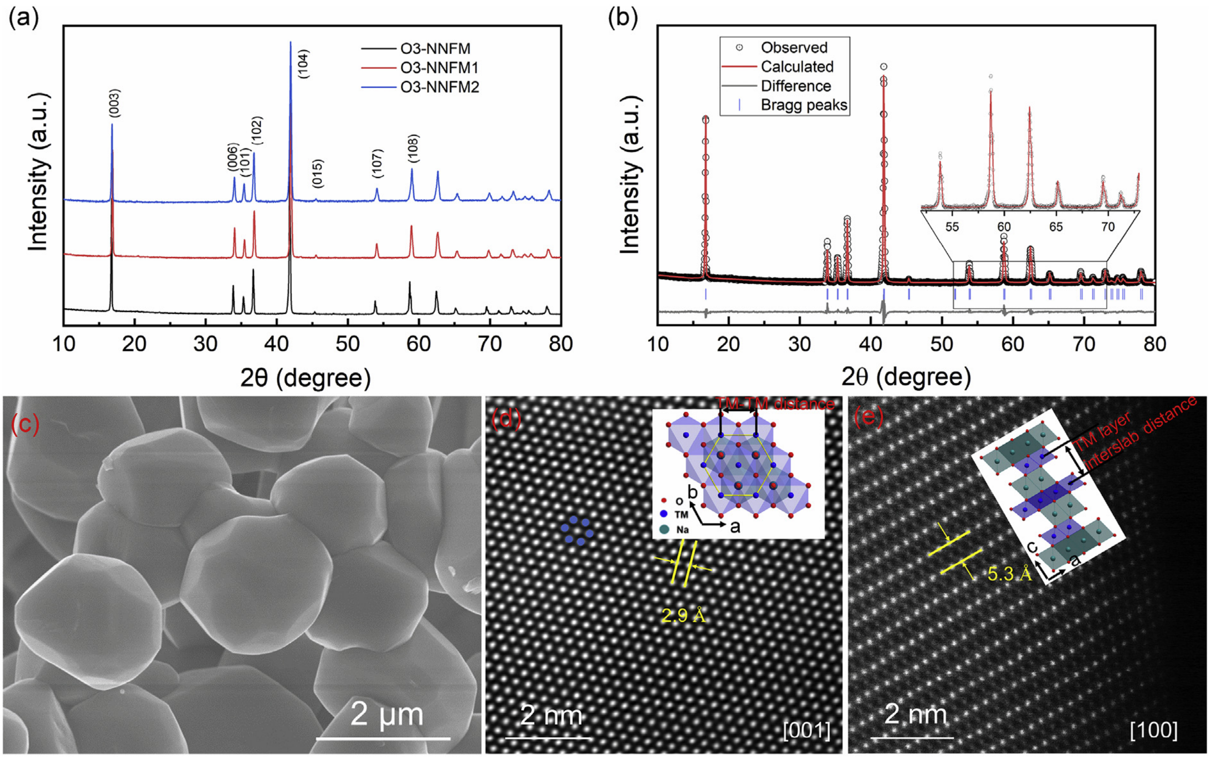

Fig. 1. Structural characterizations of the as-prepared O3 samples. (a) Powder XRD patterns of the as-prepared O3 materials. (b) Rietveld refinement pattern of the powder XRD data for O3-NNFM. (c) SEM image of O3-NNFM. (d, e) HAADF-STEM images of O3-NNFM from different directions, the inset shows crystal structure illustration of this O3-type oxide.

shown in Fig. S1. It is shown that multiple phase transitions (O′3-O′′′′3-P′3-P″3-O″3-O‴3-P‴3) during the Na^+ deintercalation are responsible for the irreversible capacity loss [17,18], thus this intrinsic structural instability renders its application in NIBs. Replacing the total Ni^{3+} with 0.5 mol Ni^{2+} and 0.5 mol Mn^{4+} per unit to obtain the hexagonal $NaNi_{0.5}Mn_{0.5}O_2$ [5] shows a higher reversible capacity of 185 mAh g^{-1} up to 4.5 V. However, the material experiences a series of structure evolution (O3–O′3-P3-P′3-P3″) as well as Na^+/vacancy ordering upon charging (Fig. S1). The formation of hexagonal P3″ phase at the end of charge is highly vulnerable to the incorporation of solvent molecules in the Na layer, considering the anomalously large interslab distances (~7.0 Å) [5], which degenerates the structure reversibility and long-term cycle stability. Further study showed that a reversible capacity of 125 mAh g^{-1} could be obtained with an optimized charge/discharge cut-off voltage between 2.2 and 3.8 V, however, the capacity and cycle performance is still not satisfied. In addition, Co^{3+} and Fe^{3+} substituted $NaNi_{0.5}Co_{0.5}O_2$ [19], $NaNi_{0.5}Fe_{0.5}O_2$ [19], $NaNi_{1/3}Co_{1/3}Mn_{1/3}O_2$ [20], $NaNi_{1/3}Fe_{1/3}Mn_{1/3}O_2$ [21] are also investigated, respectively, but these materials only deliver the reversible capacity of 120–130 mAh g^{-1} below 4.0 V, corresponding to 0.5–0.55 mol Na^+ (de)intercalation from the hosts.

Inspired by the high-active and open layered framework for fast Li^+ extraction/insertion reactions of Ni-rich Li-ion cathodes, such as $LiNi_{0.6}Co_{0.2}Mn_{0.2}O_2$ [22] or $LiNi_{0.8}Co_{0.1}Mn_{0.1}O_2$ [23] with the reversible capacity of more than 200 mAh g^{-1} (up to 4.5 V *vs.* Li^+/Li), a series of Ni-rich $NaNi_xCo_yMn_zO_2$ ($x = 0.33, 0.5, 0.6, 0.8$) [24], composition-graded $NaNi_{0.61}Co_{0.12}Mn_{0.27}O_2$ and Ti-doped $Na[Ti_{0.03}(Ni_{0.6}Co_{0.2}Mn_{0.2})_{0.97}]O_2$ materials have been studied [25,26], which showed good electrochemical properties. Recently, Yang et al. [27] reported an electrochemical Li^+/Na^+ exchange strategy for Ni-rich Na-ion oxide, $Na_{0.75}Ni_{0.82}Co_{0.12}Mn_{0.06}O_2$, which exhibited a reversible capacity of 171 mAh g^{-1} in the voltage of 2.0–4.0 V. However, the synthesis of O3-type Na-intercalated layered oxide via a topological manner derived from Li-analogues cannot be easily scaled up for the industrial application, and Co is not an optimal choice for the redox center in NIBs for its high cost. In general, for the Ni-rich O3 oxides the least phase transition and minimum volume change are considered to play pivotal roles in achieving high battery performance, thus understanding the phase transitions is significant to construct reliable cathode materials.

In this work, we designed a series of Ni-rich oxide cathodes, O3–$Na[Ni_xFe_yMn_{1-x-y}]O_2$ ($x = 0.6$, 0.7 and 0.8; labeled as O3-NNFM, O3-NNFM1 and O3-NNFM2, respectively.) through an industrially feasible coprecipitation method. Replacing Co^{3+} with Fe^{3+} not only reduces the cost of cathode materials but also contributes to the specific capacity owing to the electrochemically active of Fe in O3-type $NaFeO_2$ [28] different from the inactive O3-type $LiFeO_2$. By combining advanced *in-situ* and *ex-situ* characterization techniques, a detailed structure evolution mechanism of this O3-NNFM oxide at different states of charge was revealed. The large volume change and thermodynamic instability of the high-voltage O3″ phase is found to be responsible for the inferior cycling/rate performance. To lower the charge cut-off voltage to 4.0 V, a good comprehensive performance was obtained owing to the absence of the high-voltage phase, exhibiting a reversible capacity of 152 mAh g^{-1}, approximately 84% of capacity retention after 200 cycles at 0.5C and a rate capability of 81% capacity retention at 2C. Our work provides a preview of the structure-performance relationship for O3-type Na-ion cathodes.

2. Results and discussion

The designed Ni-rich oxide compounds were prepared by a hydroxide co-precipitation method followed by high-temperature calcination, as shown in the Supporting Information in detail. It should be mentioned that the calcinated temperature and additive amount of $NaNO_3$ have been adjusted carefully to obtain the pure phase as shown in Fig. S2. According to the X-ray diffraction (XRD) patterns (Fig. 1a), all diffraction peaks can be indexed into the hexagonal O3-type layered structure (space group:

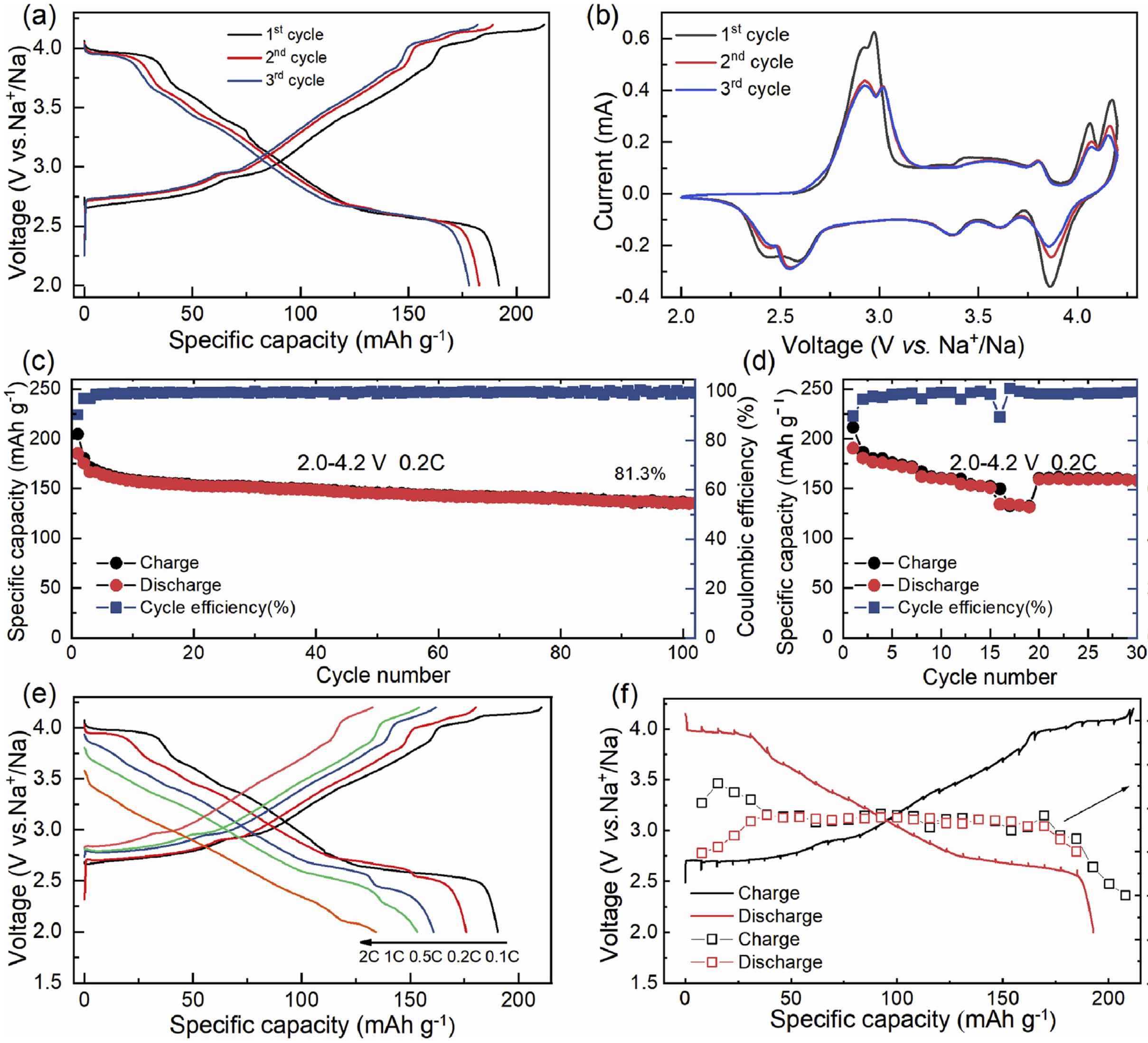

Fig. 2. Electrochemical performance of O3-NNFM cathode. (a) The galvanostatic charge/discharge curves of the O3-NNFM electrode cycled in the voltage range of 2.0–4.2 V at 0.1C. (b) CV curves of the O3-NNFM electrode at 0.1 mV s^{-1}. (c) Cycling performance of the O3-NNFM electrode in the voltage range of 2.0–4.2 V during 100 cycles at 0.2C after the initial two cycles of activation. (d, e) Rate performance of O3-NNFM electrode, galvanostatic charge/discharge curves versus specific capacity at various rates from 0.1C to 2C. (f) GITT curves of O3-NNFM cathode material in the first cycle.

$R\bar{3}m$) which is isostructural with α-$NaFeO_2$, and no other phase is recognized. The actual atomic compositions of as-prepared O3 samples were determined to be 1.030:0.594:0.253:0.153, 1.021:0.695:0.202:0.103 and 1.036:0.790:0.155:0.055 (Na: Ni: Fe: Mn), respectively, by inductively coupled plasma-atomic emission spectrometry (ICP-AES). Rietveld refinement was performed to explore the structural information of O3-NNFM as shown in Fig. 1b, and detailed crystallographic parameters were shown in Table S1. According to the obtained lattice parameters, the interslab distance of TM layer was 5.29 Å. Scanning electron microscopy (SEM) images of the O3-NNFM particles were presented in Fig. 1c and Fig. S3. Most of the particles are presented as polyhedral and ball-like morphology with an average particle size of ~2 μm and a clean surface, which are different from the common spherical morphology composed of plate/spoke-like primary particles [25,29]. The energy dispersive X-ray spectroscopy (EDS) mappings (Fig. S4) clearly reveal that all elements are homogeneously distributed on the buck of particles. The high-angle annular dark field (HAADF) scanning transmission electron microscopy (STEM) was employed to detect the atomic structure. As shown in Fig. 1d and e, the interslab distance and TM−TM distance are 5.3 Å and 2.9 Å, respectively, which are consistent with the XRD refinement results. Moreover, the clear bright-dots stretching from the particle bulk to the surface further confirms the clean surface of the pristine material and indicates favorable Na^+ transport channel.

The electrochemical performance of as-prepared O3 cathode materials was firstly evaluated by galvanostatic charge/discharge tests using pure sodium metal as counter electrode. As shown in Fig. S5, O3-NNFM and O3-NNFM1 samples show similar reversible capacity however a much smaller initial capacity for O3-NNFM2. Besides the capacity distinction, both O3-NNFM1 and O3-NNFM2 materials show even more complicated multifold oxidation/reduction steps in terms of multi-platform of capacity-voltage curve (especially in the voltage range of 3.0–4.0 V), which may seriously deteriorate long cycling performance. As a result, the O3-NNFM material displays better capacity retention during long cycling, retaining nearly >80% of the initial capacity after 100 cycles in comparison to the ~70% and 63% capacity retention for the O3-NNFM1 and O3-NNFM2 samples (Fig. S6), respectively. The possible reason could be the more Fe–Mn contents in the lattice framework of O3-NNFM, which could dramatically improve the structural stability, thus from now on, we mainly concentrate on the investigation of the structure-property relationship of O3-NNFM material.

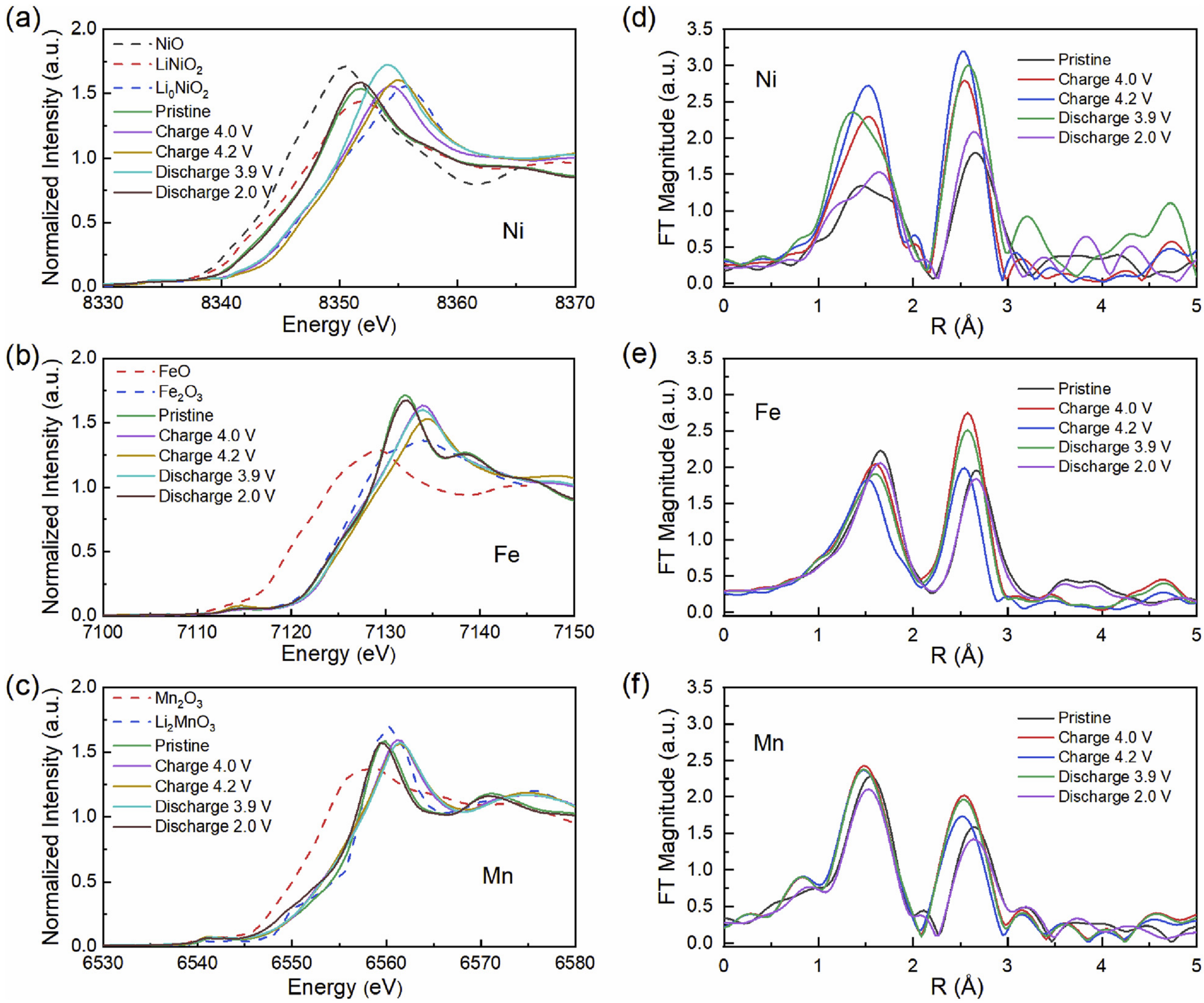

Fig. 3. Charge compensation mechanism during Na^+ (de)intercalation in O3-NNFM cathode. Normalized *ex-situ* XANES spectra at the (a) Ni K-edge, (b) Fe K-edge, (c) Mn K-edge of O3-NNFM cathode during charge/discharge and the corresponding metal oxide powders as standard references; corresponding *ex-situ* EXAFS spectra at the (d) Ni *K*-edge, (e) Fe *K*-edge, (f) Mn *K*-edge of O3-NNFM cathode during charge/discharge.

Fig. 2a displays the charge/discharge curves of the first three cycles obtained in the voltage range of 2.0–4.2 V at 0.1C (1C = 150 mA g^{-1}). The reversible capacity of 190 mAh g^{-1} is obtained with initial coulombic efficiency of ~90%, corresponding to the reversible intercalation of ~0.8 mol of Na^+ per formula unit. Such a favorable high-capacity performance leads to a specific energy of more than 584 Wh kg^{-1} (average voltage is ~3.06 V), which even surpasses the values delivered by some LIB cathodes, such as $LiFePO_4$ (about 530 Wh kg^{-1}) and $LiMn_2O_4$ (about 450 Wh kg^{-1}) [7]. It is obvious that the appearance of a long plateau above 4.0 V is responsible for the increased reversible specific capacity at a high charge cut-off voltage of 4.2 V, compared to the traditional O3-type cathode materials. This plateau is also detected in cyclic voltammetry (CV) curves with the redox peaks at 3.9/4.1 V (Fig. 2b). However, a slight capacity decay of the plateau in the second cycle is observed due to the high-voltage phase transition (discussed later). The cycle performance of the O3-NNFM electrode was tested at 0.2C after the initial two cycles. As shown in Fig. 2c, the O3-NNFM cathode retained 81.3% of the initial capacity after 100 cycles, and corresponding charge/discharge curves at selected cycles are presented in Fig. S7. It can be seen that the high-voltage plateau degraded significantly, indicating the more severe structural degradation in this region. The rate capabilities of the O3-NNFM electrode were also investigated in Fig. 2d and e, where the reversible capacities are 176, 161, 153 and 134 mAh g^{-1} at the current rates of 0.2C, 0.5C, 1C and 2C, respectively. It is worth noting that the high-voltage plateau gradually disappeared with the increasing of current rate, further confirming the inferior Na^+ diffusion kinetics at high-voltage region. In addition, the diffusion coefficient of Na^+ (D_{Na+}) was estimated using the galvanostatic intermittent titration technique (GITT), which is a common electrochemical technique to analyze diffusivities of alkali ions in electrodes [30]. As shown in Fig. 2f and S8, the apparent Na^+ diffusion coefficient for the O3-NNFM was around 6.6×10^{-11} cm^2 s^{-1} within the voltage window of 2.5–4.0 V and around 1.2×10^{-12} cm^2 s^{-1} within the voltage window of 4.0–4.2 V. Note that, the value for high-voltage phase is one fifth of those for low voltage phases, which could be attributed to the discrepant structure change.

Ex-situ X-ray absorption spectroscopy (XAS) spectra were collected at *K* edge of Ni, Fe and Mn to understand the charge compensation mechanism and the evolution of local structure during Na^+ (de)intercalation. Fig. 3a–c shows the normalized X-ray absorption near edge structure (XANES) spectra of Ni, Fe, and Mn *K*-edges at different charge and discharge states and the corresponding metal oxide powders as standard references. Similar edge positions are compared in XANES with the standard TM oxides including Ni_2O_3, Fe_2O_3, and Li_2MnO_3, indicating that the valence states of Ni, Fe, and Mn for pristine O3-NNFM are primarily determined as +3, +3, and +4, respectively. As mentioned above,

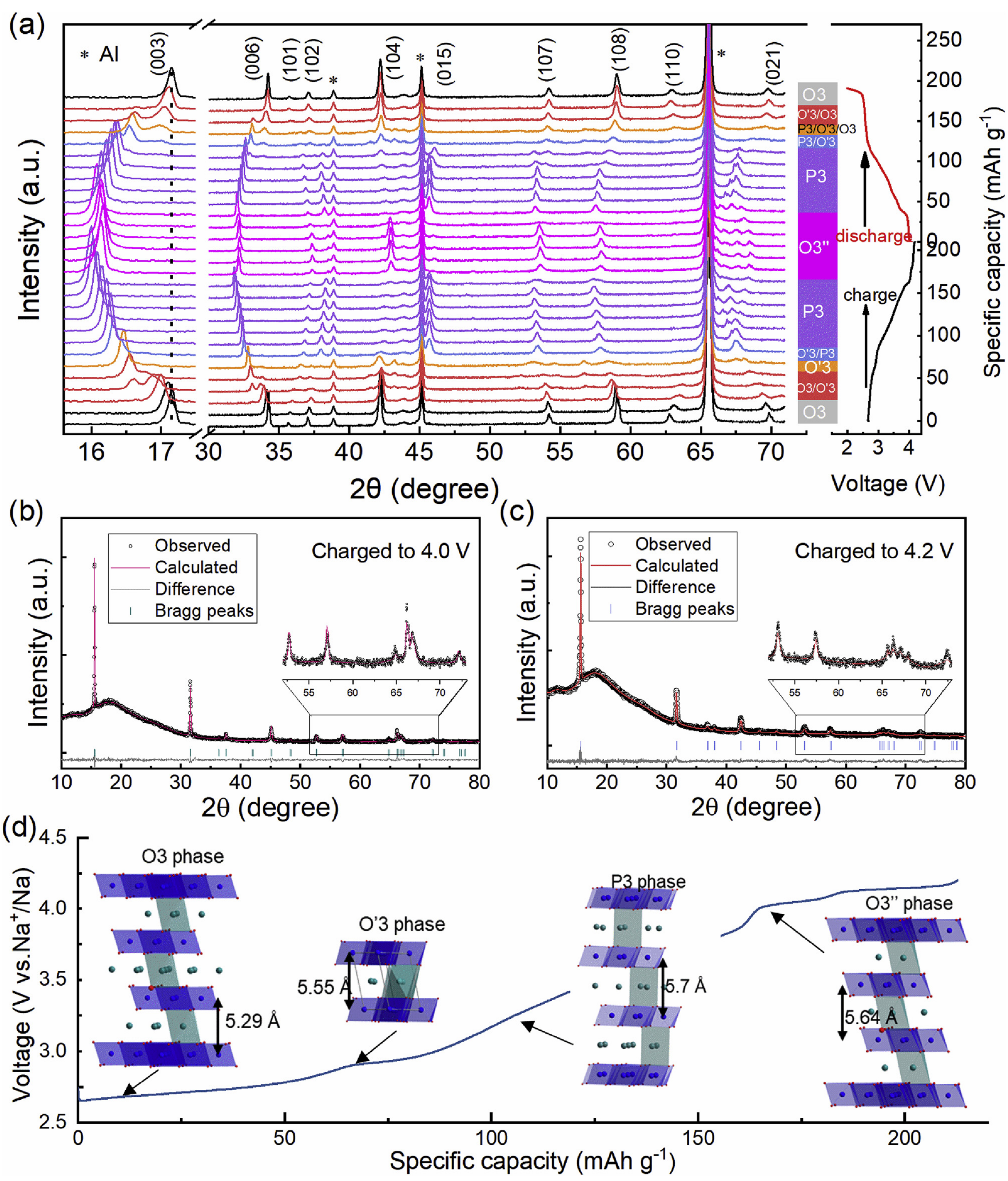

Fig. 4. Structural evolution during charge/discharge. (a) *In-situ* XRD patterns collected during the first cycle at 0.1C within the voltage range of 2.0–4.2 V for $Na_{1-x}Ni_{0.65}Fe_{0.25}Mn_{0.15}O_2$ in Na half cell. Corresponding phases and voltage-capacity profile are given on the right side. XRD patterns were collected for every change in Na stoichiometry of 0.03. (b) and (c) the Rietveld refinement patterns of the powder XRD data for O3-NNFM cathode charged to 4.0 V and 4.2 V. (d) Corresponding crystal structure evolution of O3-NNFM at different charged states.

the average valence state of TM ions in this system should be +3, thus, a certain amount of Ni^{2+} should exist in the as-prepared material to balance the total charge, which was further confirmed by X-ray photoelectron spectroscopy (XPS) results (a mixture of Ni^{3+} and Ni^{2+} with a ratio of 75:25 was confirmed as seen in Fig. S9). The Ni and Fe *K*-edge spectra have an identical tendency that a much clearer shift towards the higher energy region from initial state to 4.0 V and 4.2 V. In contrast, for the Mn *K*-edge, only small shift of the edge position is observed in the region of 2.0–4.2 V, which ascribes to the local environment changes around Mn during the Na^+ (de)intercalation process [31]. All of the TM *K*-edge shifts are highly reversible upon discharge. These results indicate that the oxidization/reduction of Ni-ion and Fe-ion are mainly responsible for the

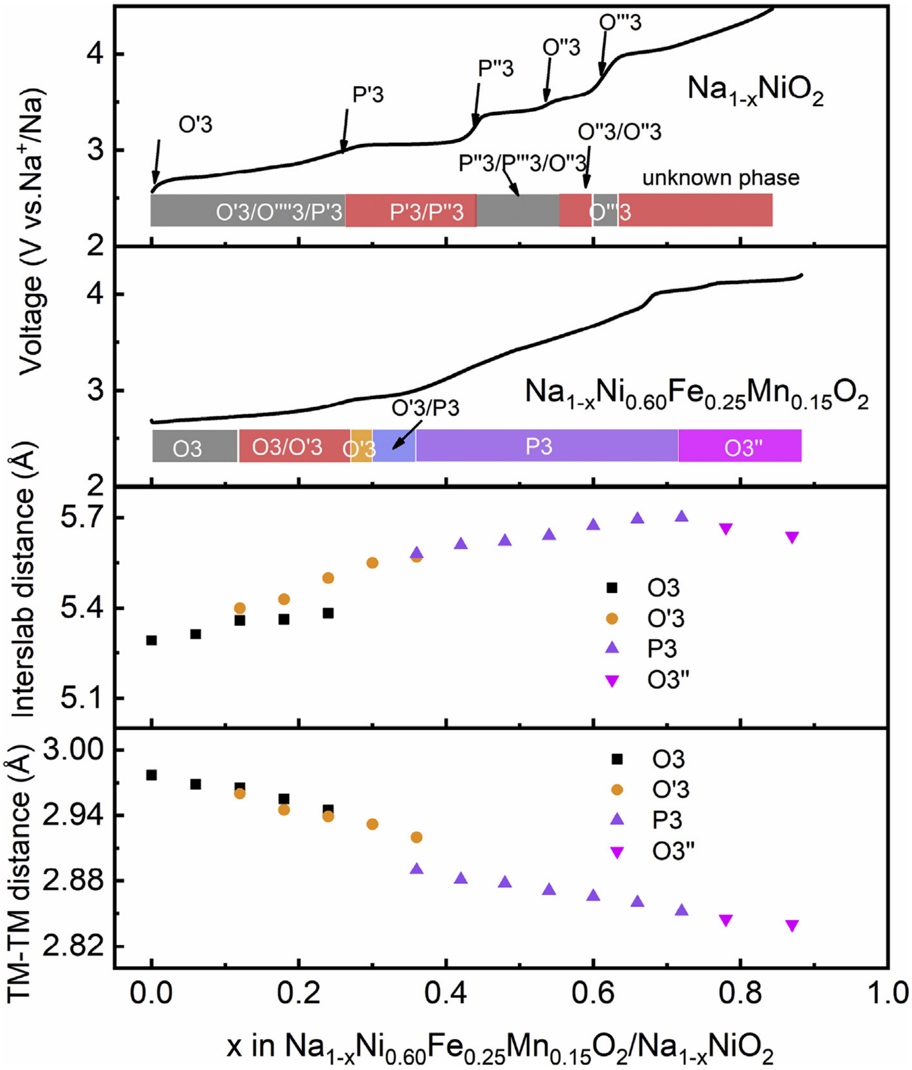

Fig. 5. Evolution of the TM-TM and interslab distances as a function of Na concentration and the phase evolution of the $Na_{1\text{-}x}Ni_{0.65}Fe_{0.25}Mn_{0.15}O_2$ system during charging process. The phase evolution of $Na_{1\text{-}x}NiO_2$ cathode is shown for comparison (top). The TM-TM and interslab distances of hexagonal and monoclinic lattice are calculated based on the relation [20]: interslab distances = $c_{hex}/3 = c_{mon}\sin\beta$; TM-TM distances = $a_{hex} = b_{mon}$.

charge compensation. The corresponding magnitudes of the Fourier transformed extended X-ray absorption fine structure (FT-EXAFS) spectra are presented in Fig. 3d–f. The two intense peaks in the Ni, Fe, and Mn *K*-edges are observed, which correspond to the average TM-O length of the first shell TM-O_6 configuration and the TM-TM length of the second shell TM-TM_6 on the *ab* plane, respectively. In the Ni *K*-edge EXAFS spectra (Fig. 3d), the peak for the first coordination shell of pristine sample splits into two parts, indicating that $Ni^{3+}(d^7)$ exhibits Jahn-Teller distortion with contributions from four O atoms at the short distance and two O atoms at the long distance [32]. With the voltage increases to 4.0 V and 4.2 V, the split peaks merge into one and its amplitude is significantly greater than that of Ni^{3+}, which means that Ni^{3+} is continuously oxided to Ni^{4+} with the absence of Jahn-Teller distortion. During the subsequent discharge, Ni-ion is reversibly reduced to its initial state, even though the bond-length changes are not completely reversible. The reason could be the slightly decreased site symmetry of Ni-ion after completing one cycle. Fig. 3e shows that the Fe–O bond length undergoes a reversible decrease/increase upon desodiation/sodiation, indicating the Fe^{3+}/Fe^{4+} oxidation/reduction. For Mn–O bond, subtle variations were only observed up to 4.2 V, and the Mn–O interatomic distance of fully sodiated sample shows negligible change compared with pristine sample, which reveals that no Mn^{4+} is involved in the charge compensation during discharging process. As for the second coordination shells, all of the TM-TM interatomic distances decrease with the oxidation of TM-ions and increase with the reduction of TM-ions, indicating a random and uniform distribution of TM-ions.

To further understand the structure evolution of this as-prepared material during Na^+ (de)intercalation process, *in-situ* XRD patterns were collected at 0.1C within the voltage range of 2.0–4.2 V (Fig. 4a and S10). Upon the initial Na^+ deintercalation (~0.12 mol), the (003) peak of the O3 phase primarily shifts to a lower angle and then a new peak representing the monoclinic O′3 phase (space group: *C*2/*m*) appeared, indicating a two-phase reaction with the coexistence of the O3 and O′3 phases in the x (Na^+ intercalation amount) range of 0.12–0.26. Note that the monoclinic distortion observed in intermediate O′3 phase is consistent with the previously reported for $NaNi_{0.5}Mn_{0.5}O_2$ [5]. The pure O′3 phase is only observed at $x = 0.3$ as shown in Fig. S11, and another biphasic domain (O′3+P3) corresponding to a value of $0.3 < x < 0.36$ readily appears. Upon further desodiation, the hexagonal P3 phase (space group: *R*3*m*) peaks show a continuous shift, where the (003), (006), (107), and (108) diffraction peaks shift towards a lower angle while the (101) and (102) peaks move towards a higher angle until charging to 4.0 V as shown in Fig. 4b, which demonstrates a solid-solution reaction with the expansion of c-axis and contraction of the ab-plane and is consistent with the electrochemical behaviour. By contrast, when the charging process is conducted above 4.0 V, the formed P3 phase undergoes a phase

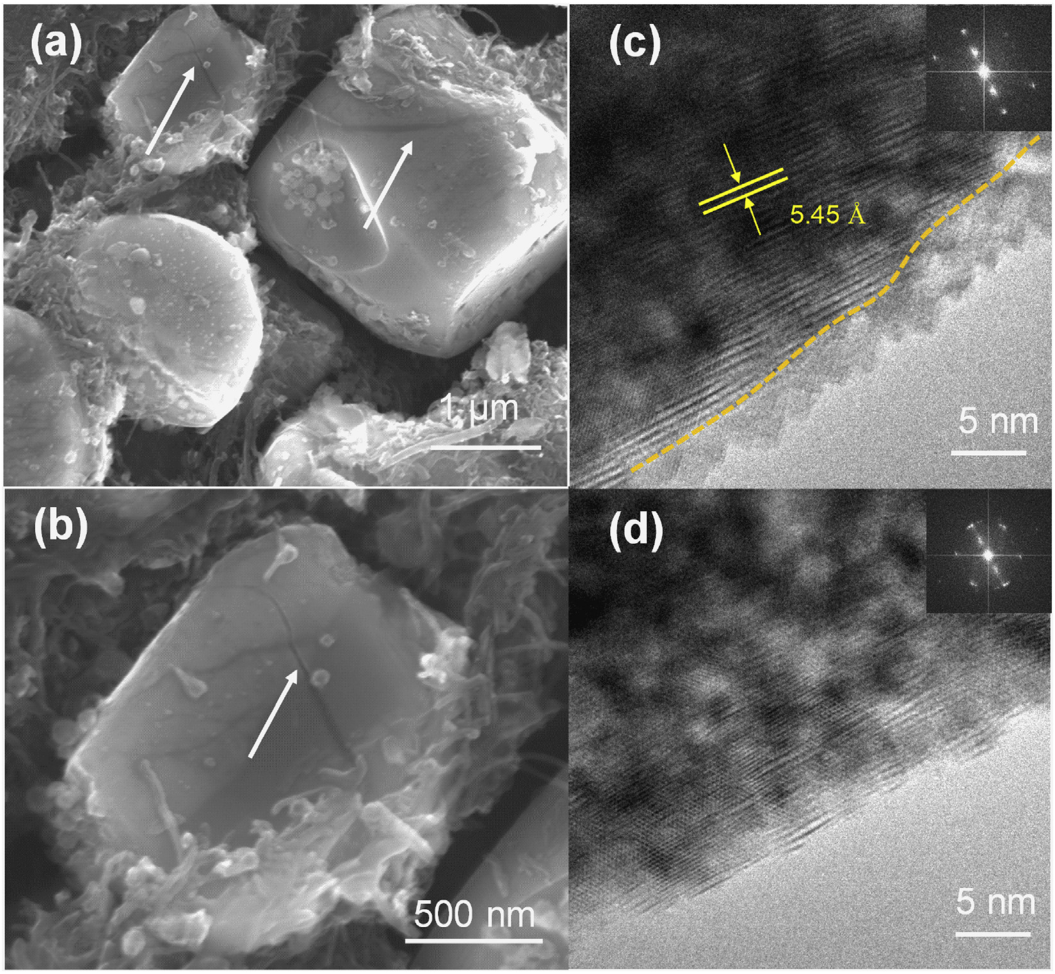

Fig. 6. Structure and morphology characterization of O3-NNFM particles after the cycling test. The SEM images (a, b) and HRTEM images (c, d) with FFT maps of O3-NNFM particles after 100 cycles in the voltage range of 2.0–4.2 V.

transition from P3 to O3″ phase via a biphasic process occurring over a narrow Na composition region (<0.03), indicating that the nucleation of O-type stacking in the P phase is more favorable when less Na^+ is reserved in the van der Waals gap [33]. This new O3″ phase is indexed to hexagonal phase with (00*l*) peaks locating at higher angles and has a higher (104)/(015) peak intensity ratio compared to the P3 phase (shown in Fig. 4c), which is similar to the pristine O3 structure but with different cell parameters owing to the much less Na content. During the further charging process, (00*l*) peaks of O3″ phase continue to shift to higher angle upon ~0.15 mol Na^+ being deintercalated out of the host structure, which indicates a solid-solution reaction until the end of charge. It is noticed that (00*l*) peaks of O3″ phase are still on the left side of the initial phase after fully desodiation, which is quite different from the recent literature results showing that the first peak ($(001)_{mon}$ or $(003)_{hex}$) of high voltage phase shifts to higher angles compared to the pristine one, such as $NaNi_{1/3}Fe_{1/3}Mn_{1/3}O_2$ [34], $NaNi_{0.5}Mn_{0.4}Ti_{0.1}O_2$ and $NaNi_{0.4}Cu_{0.1}Mn_{0.4}Ti_{0.1}O_2$ [33], usually attributing to the cation migration. This result suggests the suppression of TM-ion migration from the octahedral site in the TM layer to the neighbouring tetrahedral site of the Na layer [35]. Up to now, all of the phase transitions (O3–O′3-P3-O3″) are based on the gliding mechanism of TMO_2 [5,31], and the entire structural evolution is illustrated in Fig. 4d. The variations in the TM−TM and interslab distances calculated from Rietveld refined lattice parameters are plotted in Fig. 5, allowing a more quantitative description of the structural changes. Compared to $NaNiO_2$, a series of structural changes are significantly reduced due to the stabilizing effect of Fe^{3+} and Mn^{4+} within the structure. The interslab distance increases firstly and then decreases in a little small magnitude at the end of charging, which can be attributed to the increased electrostatic repulsion between adjacent oxygen layers owing to the removal of Na^+ and the shift of TMO_2 layers upon deep desodiation, respectively.. The TM-TM distance decreases continuously upon charging, which is consistent with the EXAFS observation due to the contraction of the TM octahedral upon TM oxidation to a higher valence state.

During the discharging process, the electrodes undergo an opposite evolution and recover to the original structure after one full cycle, indicating the high reversibility of Na^+ storage mechanism. However, as mentioned above, the plateau above 4.0 V had poor cycling stability and rate property. Therefore, to investigate the reason for such differences of durability below and above 4.0 V, the structural information of the sample charged to 4.0 V and 4.2 V are also investigated with the *ex-situ* XRD data as shown in Fig. 4b and c and Tables S2 and S3. First, the obtained P3 and O3″ phases are indexed to hexagonal structure (as well as O3 phase, in which three TMO_2 slabs are in a unit cell), and show about 0.6% and 2.7% cell volume reduction, respectively, as compared to pristine O3-NNFM. Such a large volume change in the high-voltage phase most likely accounts for the poor cycling and rate property of this compound over the extended voltage window of 2–4.2 V as seen before (Fig. 2c and d). Furthermore, the high-voltage O3″ phase would show sluggish Na^+ diffusion kinetics, which is consistent with our GITT results, therefore the stress and mechanical degradation of the electrode material are prominently accelerated during cycling. Second, in order to distinguish the structural stability of the two desodiation phases, we have embarked on a comparative study of the XRD evolution along with the

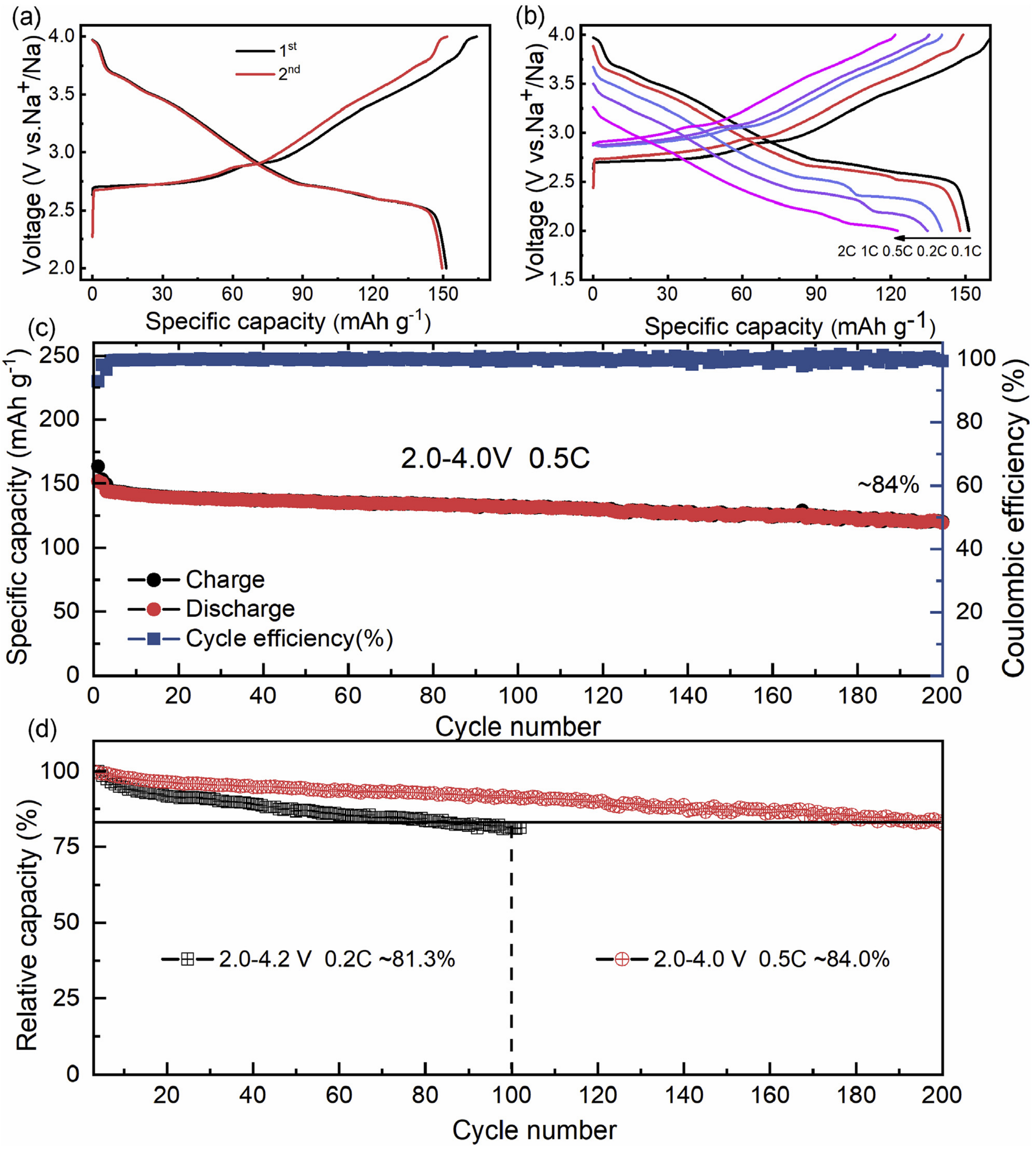

Fig. 7. Electrochemical performance of the O3-NNFM cathode in voltage range of 2.0–4.0 V. (a) The first and second galvanostatic charge and discharge curves of the O3-NNFM electrode at 0.1C. (b) Rate performance, galvanostatic charge/discharge curves versus specific capacity at various rates from 0.1C to 2C. (c) cycling performance of the O3-NNFM electrode during 200 cycles at 0.5C after the initial two cycles of activation. (d) Capacity retention ratio of O3-NNFM electrode cycled in the voltage range of 2.0–4.0 V and 2.0–4.2 V, respectively.

exposure time in ambient humidity (Figs. S12 and S13). Upon exposure to moisture, the O3″ phase quickly transformed into birnessite-like $Na_xTMO_2 \cdot nH_2O$ with water molecules lie between the layers [33,36], while the P3 phase shows quite less reactivity. The frustrating thermodynamic stability of O3″ phase undoubtedly influences the structural stability during long-term electrochemical cycling, such as the intercalation of trace amounts of water, solvent molecules and/or salt ions in the interstitial space between the TMO_2 slabs [37].

To confirm the above points, XRD measurements on the fully discharged O3-NNFM cathode after the charge/discharge cycling were conducted. As shown in Fig. S14, the XRD pattern is very complex with the first peak splitting into two and shifting to lower angles, which might be indexed to the two-phase coexistence of O′3 and P3 phase. This suggests that the initial O3 structure cannot return back and gradually transforms to O′3 and P3 phase during cycling, possibly because the intercalation of external ions prevents Na^+ from being embedded. Unfortunately, the phase transition at high voltages accompanied by larger mechanical strain causes mechanical failure of the cathode particle and

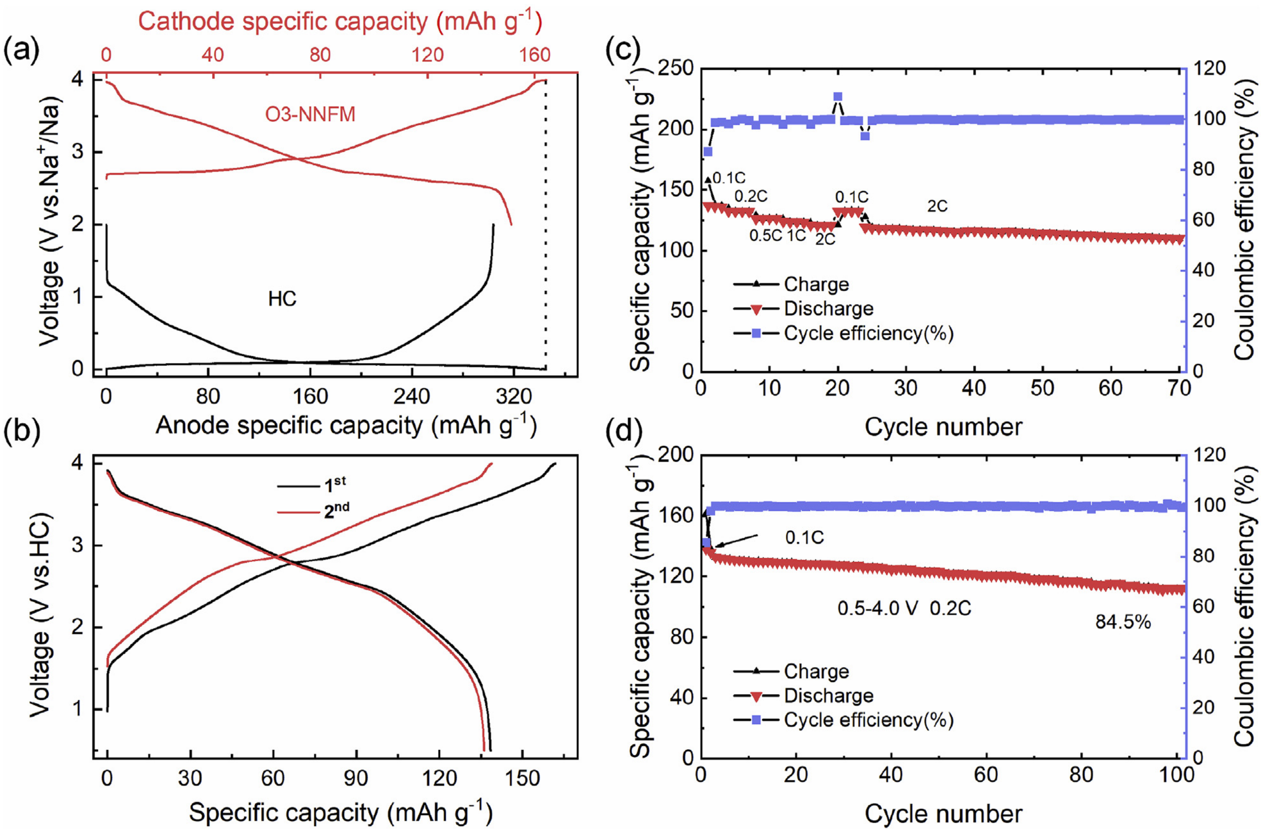

Fig. 8. Electrochemical properties of O3-NNFM//HC full cells. (a) Charge/discharge curves of the as-prepared cathode and hard carbon anode vs. Na^+/Na. The hard carbon anode shows a reversible capacity of ~300 mAh g^{-1} at a current rate of 0.1C in the voltage range of 0–2.0 V, and the first discharge capacity is used to pair the full cells. (b) Charge/discharge curves of the full cell cycled at a rate of 0.1C in the voltage range of 0.5–4.0 V. (c) Rate performance of O3-NNFM//HC full cell at various rates. (d) Retention of the discharge capacity and Coulombic efficiency at the rate of 0.2C calculated based on the mass of O3-NNFM cathode.

thus creating obvious cracks on the surface of O3-NNFM particles. As predicted, the SEM images of the cycled O3-NNFM cathode (Fig. 6a and b) show that distinct tiny microcracks appear along the particle surface. Similar microcracks could be often observed in O3-type layered lithium-ion compounds, such as $LiNi_{0.885}Co_{0.1}Al_{0.015}O_2$ and Li_xCoO_2 [38,39], when cycled at a high cut-off voltage. The local structure of the cycled O3-NNFM cathode was further analyzed by high-resolution transmission electron microscope (HRTEM) and diffraction information extracted from the TEM images by a Fourier transform. The HRTEM images along the [100] and [001] zone axis of cycled O3-NNFM particle (Fig. 6c and d) show the presentation of multiphase intergrowth and the increased interslab distance to 5.45 Å, which is in accordance with *ex-situ* XRD patterns with characteristic of the mixed P3 and O′3 structure. The corresponding fast Fourier transform in the inset further presents that the structural integrity of the cycled electrode is severely changed after long-term cycling. It is worth noting that the electrode material cycled at 4.2 V exhibits a thin layer of cathode-electrolyte interphase (CEI) along the (00*l*) surface, which is due to the interfacial side reactions and thermodynamic instability of the electrolyte during the charge/discharge. These results confirm that charging the O3-type cathode material to a high cut-off voltage not only arouses a greater degree of phase transition with a much huger volume change, but also accelerates the unfavourable solvent intercalation.

Under such circumstances, the best compromise in terms of electrode comprehensive performance is to utilize the electrode in the voltage range of 2.0–4.0 V. As shown in Fig. 7a, the initial Coulombic efficiency increased slightly from 90% to 92% when the charge voltage was limit from 4.2 to 4.0 V, which could be due to the highly reversible structural evolution and restrained electrolyte decomposition at the cathode surface. Moreover, the material exhibited a reversible specific capacity of 152 mAh g^{-1}, corresponding to an energy density of 447 Wh kg^{-1} (average voltage is ~2.95 V). The high reversibility of Na^+ (de)intercalation was also evidenced by the close overlapping of the galvanostatic charge and discharge curves. The rate capabilities were investigated at varied current rates as shown in Fig. 7b; the reversible capacities were 152, 148, 140, 135 and 123 mAh g^{-1} at the current densities of 0.1C, 0.2C, 0.5C, 1C and 2C, respectively. To further confirm the high rate capability of O3-NNFM, the Na^+ diffusion coefficient of the cathode was also evaluated by CV measurement. The Na^+ diffusion coefficient (D_{Na+}) values are calculated to be about 5.2×10^{-11} and 4.3×10^{-11} cm^2 s^{-1} for the cathodic and anodic peaks, respectively, which are well consistent with the value obtained from GITT measurement for low voltage phases, and calculation details are provided in Supporting Information (Fig. S15). For the long-term cycling stability, when tested at 0.2C and 0.5C, the O3-NNFM cathode displayed capacity retentions of 90% and 84% after 100 and 200 cycles, respectively (Figs. S16 and 7c), demonstrating the excellent reversibility with a lower charge cut-off voltage (Fig. 7d). We have also summarized the electrochemical properties of several similar O3-type layered transition metal oxide cathode materials (Table S4), the integrated performance of the as-prepared O3-NNFM material in terms of capacity, cycle retention and high rate capability is remarkable among its peers.

The structural stability of the O3-NNFM cathode was also verified by *in-situ* XRD test in the voltage range of 2.0–4.0 V. The evolution of the XRD patterns (Fig. S17) shows that the phase transitions observed during charging up to 4 V correspond to the O3–O′3-P3 sequences, and a thorough reversible behaviour is observed during the discharging process. In general, O3-type structure transforms into P3-type one after moderate Na extraction, and then evolves into another O3-type phase when the electrode materials have more than 0.5 mol Na^+ extraction, as confirmed in previous literature. This value has improved to 0.6 for $NaFe_{1/2}Co_{1/2}O_2$ [40,41], $NaNi_{1/3}Fe_{1/3}Co_{1/3}O_2$ [42], $NaNi_{1/3}Fe_{1/3}Mn_{1/3}O_2$ [43], and $NaNi_{1/4}Fe_{1/4}Co_{1/4}Mn_{1/4}O_2$ [44]. Interestingly, after 0.68 mol Na^+ being extracted in O3-NNFM, the P3 phases can still be maintained according to the *in-situ* and *ex-situ* XRD data (Fig. 4b), which could be responsible for the remarkable reversible specific capacity and excellent cycle performance. Furthermore, the O3 phase with hexagonal symmetry was still maintained even after 200 cycles and no crack was found on the surface of cathode particles (as shown in Figs. S18 and S19), suggesting that the electrochemical reactions in the resultant O3-NNFM material are highly reversible in this voltage range, which could contribute to the impressive cycling stability (~84% capacity retention after 200 cycles).

To further investigate the O3-NNFM cathode in practical application, full cell was fabricated with hard carbon (HC) as anode (Fig. 8a and Fig. S20) and measured by galvanostatic charge/discharge cycling at various rates in the voltage range of 0.5–4.0 V. As shown in Fig. 8b, the full cell can deliver a specific capacity of 138 mAh g^{-1}, corresponding to an energy density of 256 Wh kg^{-1} (based on the total mass of cathode and anode active materials). The initial Coulombic efficiency is about ~85.5%, and >99.5% after several cycles. As shown in Fig. 8c the full cell can deliver rate capacities of 138 mAh g^{-1}, 132 mAh g^{-1}, 126 mAh g^{-1}, 123 mAh g^{-1}, 121 mAh g^{-1} at 0. 1C, 0.2C, 0.5C, 1.0C, and 2.0C, respectively, verifying the highly stable and reversible reactions of O3-NNFM cathode material again. Besides, the cycling performance of the coin-type full cell has also been tested and 84% capacity was attained at 0.2C over one hundrad cycles(Fig. 8d), which demonstrates excellent cycling stability and a great commercial prospect for practical NIBs.

3. Conclusions

In summary, we report a novel O3-type Na-ion layered oxide material, $Na[Ni_{0.60}Fe_{0.25}Mn_{0.15}]O_2$, which was synthesized by an industrially feasible coprecipitation method. A combination of *ex-situ* XAS and *in-situ* XRD analyses was performed to inversigate the reaction mechanism, which demonsdated that nickel and iron cations are mainly involved in the charge compensation mechanism with a highly reversible O3–O′3-P3-O3″ phase transition upon Na^+ (de)intercalation. It is worth noting that the high-voltage O3″ phase displayed inferior Na^+ diffusion kinetics and thermodynamic stability, as revealed by GITT, *ex-situ* XRD and TEM analysis. By decreasing the charge voltage from 4.2 to 4.0 V, in the absence of the high-voltage O3″ phase, the electrode exhibits an excellent comprehensive performance (approximately 84% of capacity retention after 200 cycles and the good rate capability with approximately 81% of capacity retention at 2.0C). Furthermore, the confirmed deterioration mechanism in the high voltage helps clarify the capacity decay reason and drive the pursuit of effective solutions. We hope feasible strategies could be implemented in the future, such as surface coating, trace doping or electrolyte optimization for the development of stable and high-capacity cathode material for NIBs.

Declaration of competing interest

The authors declared that they have no conflicts of interest to this work.

Acknowledgements

This work was supported by the National Natural Science Foundation of China (51725206 and 51421002), the Strategic Priority Research Program of the Chinese Academy of Sciences (XDA21070500), Beijing Municipal Science and Technology Commission (Z181100004718008) and Beijing Natural Science Fund-Haidian Original Innovation Joint Fund (L182056).

Appendix A. Supplementary data

Supplementary data to this article can be found online at https://doi.org/10.1016/j.ensm.2020.05.013.

References

[1] Y.-S. Hu, Y. Lu, 2019 nobel prize for the Li-ion batteries and new opportunities and challenges in Na-ion batteries, ACS Energy Lett. 4 (2019) 2689–2690.

[2] N. Yabuuchi, K. Kubota, M. Dahbi, S. Komaba, Research development on sodium-ion batteries, Chem. Rev. 114 (2014) 11636–11682.

[3] C. Zhao, Y. Lu, L. Chen, Y.-S. Hu, Ni-based cathode materials for Na-ion batteries, Nano Res. 12 (2019) 2018–2030.

[4] C. Zhao, Z. Yao, Q. Wang, H. Li, J. Wang, M. Liu, S. Ganapathy, Y. Lu, J. Cabana, B. Li, X. Bai, A. Aspuru-Guzik, M. Wagemaker, L. Chen, Y.-S. Hu, Revealing high Na-content P2-type layered oxides as advanced sodium-ion cathodes, J. Am. Chem. Soc. 142 (2020) 5742–5750.

[5] S. Komaba, N. Yabuuchi, T. Nakayama, A. Ogata, T. Ishikawa, I. Nakai, Study on the reversible electrode reaction of $Na_{(1-x)}Ni_{0.5}Mn_{0.5}O_2$ for a rechargeable sodium-ion battery, Inorg. Chem. 51 (2012) 6211–6220.

[6] L. Mu, S. Xu, Y. Li, Y.S. Hu, H. Li, L. Chen, X. Huang, Prototype sodium-ion batteries using an air-stable and Co/Ni-free O3-layered metal oxide cathode, Adv. Mater. 27 (2015) 6928–6933.

[7] C. Zhao, F. Ding, Y. Lu, L. Chen, Y.-S. Hu, High-entropy layered oxide cathodes for sodium-ion batteries, Angew. Chem. Int. Ed. 59 (2020) 264–269.

[8] Q. Wang, W. Yang, F. Kang, B. Li, $Na_2Mn^{3+}{}_{0.3}Mn^{4+}{}_{2.7}O_{6.85}$: a cathode with simultaneous cationic and anionic redox in Na-ion battery, Energy Storage Mater. 14 (2018) 361–366.

[9] Y. Qi, Z. Tong, J. Zhao, L. Ma, T. Wu, H. Liu, C. Yang, J. Lu, Y.-S. Hu, Scalable room-temperature synthesis of multi-shelled $Na_3(VOPO_4)_2F$ microsphere cathodes, Joule 2 (2018) 2348–2363.

[10] H. Gao, I.D. Seymour, S. Xin, L. Xue, G. Henkelman, J.B. Goodenough, $Na_3MnZr(PO_4)_3$: a high-voltage cathode for sodium batteries, J. Am. Chem. Soc. 140 (2018) 18192–18199.

[11] M. Bianchini, F. Fauth, N. Brisset, F. Weill, E. Suard, C. Masquelier, L. Croguennec, Comprehensive investigation of the $Na_3V_2(PO_4)_2F_3$–$NaV_2(PO_4)_2F_3$ system by operando high resolution synchrotron X-ray diffraction, Chem. Mater. 27 (2015) 3009–3020.

[12] C. Zhao, Z. Yao, D. Zhou, L. Jiang, J. Wang, V. Murzin, Y. Lu, X. Bai, A. Aspuru-Guzik, L. Chen, Y.-S. Hu, Constructing Na-ion cathodes via alkali-site substitution, Adv. Funct. Mater. (2020) 1910840.

[13] L. Wang, J. Song, R. Qiao, L.A. Wray, M.A. Hossain, Y.D. Chuang, W. Yang, Y. Lu, D. Evans, J.J. Lee, S. Vail, X. Zhao, M. Nishijima, S. Kakimoto, J.B. Goodenough, Rhombohedral prussian white as cathode for rechargeable sodium-ion batteries, J. Am. Chem. Soc. 137 (2015) 2548–2554.

[14] Y. You, X. Yu, Y. Yin, K.-W. Nam, Y.-G. Guo, Sodium iron hexacyanoferrate with high Na content as a Na-rich cathode material for Na-ion batteries, Nano Res. 8 (2014) 117–128.

[15] W. Pan, W. Guan, S. Liu, B.B. Xu, C. Liang, H. Pan, M. Yan, Y. Jiang, $Na_2Fe(SO_4)_2$: an anhydrous 3.6 V, low-cost and good-safety cathode for a rechargeable sodium-ion battery, J. Mater. Chem. A 7 (2019) 13197–13204.

[16] P. Vassilaras, X. Ma, X. Li, G. Ceder, Electrochemical properties of monoclinic $NaNiO_2$, J. Electrochem. Soc. 160 (2012) A207–A211.

[17] L. Wang, J. Wang, X. Zhang, Y. Ren, P. Zuo, G. Yin, J. Wang, Unravelling the origin of irreversible capacity loss in $NaNiO_2$ for high voltage sodium ion batteries, Nano Energy 34 (2017) 215–223.

[18] M.H. Han, E. Gonzalo, M. Casas-Cabanas, T. Rojo, Structural evolution and electrochemistry of monoclinic $NaNiO_2$ upon the first cycling process, J. Power Sources 258 (2014) 266–271.

[19] P. Vassilaras, D.-H. Kwon, S.T. Dacek, T. Shi, D.-H. Seo, G. Ceder, J.C. Kim, Electrochemical properties and structural evolution of O3-type layered sodium mixed transition metal oxides with trivalent nickel, J. Mater. Chem. A 5 (2017) 4596–4606.

[20] M. Sathiya, K. Hemalatha, K. Ramesha, J.M. Tarascon, A.S. Prakash, Synthesis, structure, and electrochemical properties of the layered sodium insertion cathode material: $NaNi_{1/3}Mn_{1/3}Co_{1/3}O_2$, Chem. Mater. 24 (2012) 1846–1853.

[21] M. Jeong, H. Lee, J. Yoon, W.-S. Yoon, O3-type $NaNi_{1/3}Fe_{1/3}Mn_{1/3}O_2$ layered cathode for Na-ion batteries: structural evolution and redox mechanism upon Na (de) intercalation, J. Power Sources 439 (2019) 227064.

[22] W. Liu, X. Li, D. Xiong, Y. Hao, J. Li, H. Kou, B. Yan, D. Li, S. Lu, A. Koo, K. Adair, X. Sun, Significantly improving cycling performance of cathodes in lithium ion batteries: the effect of Al_2O_3 and $LiAlO_2$ coatings on $LiNi_{0.6}Co_{0.2}Mn_{0.2}O_2$, Nano Energy 44 (2018) 111–120.

[23] X. Xiong, Z. Wang, P. Yue, H. Guo, F. Wu, J. Wang, X. Li, Washing effects on electrochemical performance and storage characteristics of $LiNi_{0.8}Co_{0.1}Mn_{0.1}O_2$ as cathode material for lithium-ion batteries, J. Power Sources 222 (2013) 318–325.

[24] J.-Y. Hwang, C.S. Yoon, I. Belharouak, Y.-K. Sun, A comprehensive study of the role of transition metals in O3-type layered $Na[Ni_xCo_yMn_z]O_2$ ($x = 1/3$, 0.5, 0.6, and 0.8) cathodes for sodium-ion batteries, J. Mater. Chem. A 4 (2016) 17952–17959.

[25] J.Y. Hwang, S.M. Oh, S.T. Myung, K.Y. Chung, I. Belharouak, Y.K. Sun, Radially aligned hierarchical columnar structure as a cathode material for high energy density sodium-ion batteries, Nat. Commun. 6 (2015) 6865.

[26] T.-Y. Yu, J.-Y. Hwang, I.T. Bae, H.-G. Jung, Y.-K. Sun, High-performance Ti-doped O3-type Na[$Ti_x(Ni_{0.6}Co_{0.2}Mn_{0.2})_{1-x}$]$O_2$ cathodes for practical sodium-ion batteries, J. Power Sources 422 (2019) 1–8.

[27] J. Yang, M. Tang, H. Liu, X. Chen, Z. Xu, J. Huang, Q. Su, Y. Xia, O3-Type layered Ni-rich oxide: a high-capacity and superior-rate cathode for sodium-ion batteries, Small (2019), e1905311.

[28] E. Lee, D.E. Brown, E.E. Alp, Y. Ren, J. Lu, J.-J. Woo, C.S. Johnson, New insights into the performance degradation of Fe-based layered oxides in sodium-ion batteries: instability of Fe^{3+}/Fe^{4+} redox in α-$NaFeO_2$, Chem. Mater. 27 (2015) 6755–6764.

[29] Y. You, A. Dolocan, W. Li, A. Manthiram, Understanding the air-exposure degradation chemistry at a nanoscale of layered oxide cathodes for sodium-ion batteries, Nano Lett. 19 (2019) 182–188.

[30] Z. Shen, L. Cao, C.D. Rahn, C.-Y. Wang, Least squares galvanostatic intermittent titration technique (LS-GITT) for accurate solid phase diffusivity measurement, J. Electrochem. Soc. 160 (2013) A1842–A1846.

[31] P.F. Wang, H.R. Yao, X.Y. Liu, J.N. Zhang, L. Gu, X.Q. Yu, Y.X. Yin, Y.G. Guo, Ti-substituted $NaNi_{0.5}Mn_{0.5-x}Ti_xO_2$ cathodes with reversible O3-P3 phase transition for high-performance sodium-ion batteries, Adv. Mater. 29 (2017) 1700210.

[32] A.N. Mansour, X.Q. Yang, X. Sun, J. McBreen, L. Croguennec, C. Delmas, In situ X-ray absorption spectroscopy study of $Li_{(1-z)}Ni_{(1+z)}O_2$ ($z \leq 0.02$) cathode material, J. Electrochem. Soc. 146 (1999) 2799.

[33] Q. Wang, S. Mariyappan, J. Vergnet, A.M. Abakumov, G. Rousse, F. Rabuel, M. Chakir, J.M. Tarascon, Reaching the energy density limit of layered O3-$NaNi_{0.5}Mn_{0.5}O_2$ electrodes via dual Cu and Ti substitution, Adv. Energy Mater. 9 (2019) 1901785.

[34] Y. Xie, H. Wang, G. Xu, J. Wang, H. Sheng, Z. Chen, Y. Ren, C.-J. Sun, J. Wen, J. Wang, D.J. Miller, J. Lu, K. Amine, Z.-F. Ma, In operando XRD and TXM study on the metastable structure change of NaNi1/3Fe1/3Mn1/3O2 under electrochemical sodium-ion intercalation, Adv. Energy Mater. 6 (2016) 1601306.

[35] J. Xu, Z. Han, K. Jiang, P. Bai, Y. Liang, X. Zhang, P. Wang, S. Guo, H. Zhou, Suppressing cation migration and reducing particle cracks in a layered Fe-based cathode for advanced sodium-ion batteries, Small (2019), e1904388.

[36] M. Sathiya, Q. Jacquet, M.-L. Doublet, O.M. Karakulina, J. Hadermann, J.-M. Tarascon, A chemical approach to raise cell voltage and suppress phase transition in O3 sodium layered oxide electrodes, Adv. Energy Mater. 8 (2018) 1702599.

[37] Y. You, S. Xin, H.Y. Asl, W. Li, P.-F. Wang, Y.-G. Guo, A. Manthiram, Insights into the improved high-voltage performance of Li-incorporated layered oxide cathodes for sodium-ion batteries, Chem 4 (2018) 2124–2139.

[38] Q. Liu, X. Su, D. Lei, Y. Qin, J. Wen, F. Guo, Y.A. Wu, Y. Rong, R. Kou, X. Xiao, F. Aguesse, J. Bareño, Y. Ren, W. Lu, Y. Li, Approaching the capacity limit of lithium cobalt oxide in lithium ion batteries via lanthanum and aluminium doping, Nat. Energy 3 (2018) 936–943.

[39] H.H. Ryu, K.J. Park, D.R. Yoon, A. Aishova, C.S. Yoon, Y.K. Sun, Li [$Ni_{0.9}Co_{0.09}W_{0.01}$]$O_2$: a new type of layered oxide cathode with high cycling stability, Adv. Energy Mater. 9 (2019) 1902698.

[40] K. Amaha, W. Kobayashi, S. Akama, K. Mitsuishi, Y. Moritomo, Interrelation between inhomogeneity and cyclability in O3-$NaFe_{1/2}Co_{1/2}O_2$, Phys. Status. Solidi R 11 (2017) 1600284.

[41] K. Kubota, T. Asari, H. Yoshida, N. Yaabuuchi, H. Shiiba, M. Nakayama, S. Komaba, Understanding the structural evolution and redox mechanism of a $NaFeO_2$-$NaCoO_2$ solid solution for sodium-ion batteries, Adv. Funct. Mater. 26 (2016) 6047–6059.

[42] P. Vassilaras, A.J. Toumar, G. Ceder, Electrochemical properties of $NaNi_{1/3}Co_{1/3}Fe_{1/3}O_2$ as a cathode material for Na-ion batteries, Electrochem. Commun. 38 (2014) 79–81.

[43] H.R. Yao, W.J. Lv, Y.X. Yin, H. Ye, X.W. Wu, Y. Wang, Y. Gong, Q. Li, X. Yu, L. Gu, Z. Huang, Y.G. Guo, Suppression of monoclinic phase transitions of O3-type cathodes based on electronic delocalization for Na-ion batteries, ACS Appl. Mater. Interfaces 11 (2019) 22067–22073.

[44] X. Li, D. Wu, Y.-N. Zhou, L. Liu, X.-Q. Yang, G. Ceder, O3-type $Na(Mn_{0.25}Fe_{0.25}Co_{0.25}Ni_{0.25})O_2$: a quaternary layered cathode compound for rechargeable Na ion batteries, Electrochem. Commun. 49 (2014) 51–54.